AGU PUBLICATIONS

JGR

Journal of Geophysical Research: Space Physics

RESEARCH ARTICLE

10.1002/2017JA023995

Simultaneous Measurements of Substorm-Related Electron Energization in the Ionosphere and the Plasma Sheet

N. Sivadas[1], **J. Semeter**[1], **Y. Nishimura**[1,2], **and A. Kero**[3]

[1]Department of Electrical and Computer Engineering and Center for Space Physics, Boston University, Boston, MA, USA, [2]Department of Atmospheric and Oceanic Sciences, University of California Los Angeles, Los Angeles, CA, USA, [3]Sodankylä Geophysical Observatory and University of Oulu, Sodankylä, Finland

Key Points:
- Subrelativistic electron precipitation ≳100 keV observed using incoherent scatter radar during a substorm
- Source of the precipitating subrelativistic electrons lies at or tailward of the inner plasma sheet
- Incoherent scatter radar can measure energy spectra of precipitating magnetospheric plasma

Supporting Information:
- Supporting Information S1

Correspondence to:
N. Sivadas,
nithin@bu.edu

Citation:
Sivadas, N., Semeter, J., Nishimura, Y., & Kero, A. (2017). Simultaneous measurements of substorm-related electron energization in the ionosphere and the plasma sheet. *Journal of Geophysical Research: Space Physics*, *122*, 10,528–10,547. https://doi.org/10.1002/2017JA023995

Received 3 FEB 2017
Accepted 13 SEP 2017
Accepted article online 28 SEP 2017
Published online 13 OCT 2017

Abstract On 26 March 2008, simultaneous measurements of a large substorm were made using the Poker Flat Incoherent Scatter Radar, Time History of Events and Macroscale Interactions during Substorm (THEMIS) spacecraft, and all sky cameras. After the onset, electron precipitation reached energies ≳100 keV leading to intense *D* region ionization. Identifying the source of energetic precipitation has been a challenge because of lack of quantitative and magnetically conjugate measurements of loss cone electrons. In this study, we use the maximum entropy inversion technique to invert altitude profiles of ionization measured by the radar to estimate the loss cone energy spectra of primary electrons. By comparing them with magnetically conjugate measurements from THEMIS-D spacecraft in the nightside plasma sheet, we constrain the source location and acceleration mechanism of precipitating electrons of different energy ranges. Our analysis suggests that the observed electrons ≳100 keV are a result of pitch angle scattering of electrons originating from or tailward of the inner plasma sheet at ~9R_E, possibly through interaction with electromagnetic ion cyclotron waves. The electrons of energy 10–100 keV are produced by pitch angle scattering due to a potential drop of ≲10 kV in the auroral acceleration region (AAR) as well as wave–particle interactions in and tailward of the AAR. This work demonstrates the utility of magnetically conjugate ground- and space-based measurements in constraining the source of energetic electron precipitation. Unlike in situ spacecraft measurements, ground-based incoherent scatter radars combined with an appropriate inversion technique can be used to provide remote and continuous-time estimates of loss cone electrons in the plasma sheet.

Plain Language Summary On the night of 26 March 2008 in Alaska, the sky lit up with intense auroral activity. A ground-based electronically steerable radar and a spacecraft were simultaneously monitoring this activity. The radar observed intense signatures of charged particle density at unusually low altitudes (<70 km), suggesting that unusually high-energy electrons were raining down from the magnetosphere. Although numerous studies in the past have estimated the source population of electrons, it has been difficult to determine and separate contributions from different physical processes. In this study, we deduced the energy and number of these electrons using radar measurements of charged particle density as a function of altitude. By comparing this estimate with that measured by the spacecraft along the same magnetic field line, we identified the source location and mechanism of acceleration of electrons of different energies. Our analysis suggests that the observed high-energy electrons are accelerated at distances beyond ~60,000 km from the Earth by interacting with electromagnetic waves, whereas lower energy electrons are mostly accelerated by electric fields much closer to Earth. Our study demonstrates the utility of combining radar and spacecraft measurements in determining the source region and acceleration process of these high-energy electrons.

1. Introduction

The Earth's magnetosphere is a cosmic plasma laboratory, which enables us to investigate the fundamental physics of energy exchange between fields and particles in the universe. One major energy exchange process in the nightside magnetosphere is the magnetospheric substorm. Substorms release energy stored in the magnetotail by the solar wind (Baker et al., 1996; Lopez, 2000) into many forms including particle acceleration and precipitation into the ionosphere. Intense dawn–dusk electric fields associated with substorm dipolarization play a major role in energetic particle injections in the near-Earth plasma sheet (Birn et al., 2012; Gabrielse et al., 2012) with particle acceleration reaching up to mega-electron volt energies (Dai et al., 2015).

Accelerated particles with pitch angles within the loss cone precipitate into the ionosphere at high latitudes. The precipitating particles contain a mixture of essentially two energetic particle population one produced by the near-Earth auroral acceleration region (AAR) and the other arising from the direct precipitation of the plasma sheet electrons. The former is associated with the discrete aurora and the latter with the diffuse aurora (Mironova et al., 2015). These visual signatures, a result of ionization driven by precipitating particles, are an ionospheric reflection of energy exchange in the magnetosphere. Thus, ionospheric measurements can be used to remote sense these processes, which are difficult to quantify using in situ measurements. In this paper, we discuss source locations of electron precipitation of different energies and contributions of particle acceleration in different regions during a substorm event using the Poker Flat Incoherent Scatter Radar (PFISR) in combination with in situ measurements by the Time History of Events and Macroscale Interactions during Substorm (THEMIS) spacecraft.

The visible aurora is caused by precipitating electrons with ~1–10 keV energy (Colpitts et al., 2013; Tanskanen et al., 1981). Precipitating electron population can contain a high-energy tail of electrons of primary energies ranging from 10 to 100 keV that cause X-ray emissions (Brown, 1966). This high-energy tail, sometimes referred to as energetic electron precipitation (EEP), was first measured indirectly by rockoons (small rockets carried by balloons and ignited in the stratosphere) with onboard Geiger tubes and scintillation counters that measured the X-rays (Meredith et al., 1955). EEPs have been measured in the past using cosmic radio noise absorption by riometers (e.g., Berkey et al., 1974; Hartz & Brice, 1967), X-ray measurements from balloon campaigns (e.g., Barcus & Rosenberg, 1966; Pytte & West, 1978), ionosphere electron density measurements from incoherent scatter radar (e.g., del Pozo et al., 1993; Osepian et al., 1996), particle measurements in space (e.g., McDiarmid et al., 1975; Collis & Korth, 1985), and X-ray measurements from low-altitude satellites (e.g., Imhof et al., 1978). Simultaneous ground- and space-based observations have been used to study temporal and spatial evolution of EEPs and their source in the plasma sheet during substorms (Kosch et al., 2001; Kurita et al., 2015; Pytte & West, 1978). According to Seppälä et al. (2015), enhanced ionization from EEPs $>$30 keV caused by substorms may lead to an ozone loss of 5–50% in the mesospheric column depending on season. EEPs at lower latitudes are also a significant loss mechanism for the outer radiation belts (e.g., Morley et al., 2010; Thorne et al., 2005).

In previous literature, no consistent definition of the EEPs has been followed, as authors have chosen the definitions of electron energies depending on their foci: 10–100 (Brown, 1966), 25–100 (Anderson & Enemark, 1960), $>$30 (Lam et al., 2010), and 4.65–1,050 keV (Callis et al., 1998). In our study, we classify energy ranges of precipitating electrons based on phenomenological grounds. Electron precipitation of energies 1–10 keV is termed auroral electron precipitation, as this population is predominantly the cause of the visible aurora. We identify electron precipitation between 10 and 100 keV in the auroral region as energetic auroral electron precipitation, as this population is mostly energized and scattered by processes within the auroral acceleration region and the intervening space between the ionosphere and the plasma sheet. The upper energy limit of energetic auroral electron precipitation is limited by the maximum energization in the auroral acceleration region, which is in turn limited by the maximum polar cap potential that reaches up to ~100 kV (Borovsky, 1993; Boyle et al., 1997). As we discuss later in the paper, the precipitating electrons of energy $>$100 keV are likely to originate from sources within the plasma sheet or the magnetotail. Utilizing the fact that rest mass of an electron is 511 keV, we define electron precipitation between 100 and 500 keV as subrelativistic electron precipitation and that greater than 500 keV as relativistic electron precipitation.

However, the source of energization of electrons is not uniquely determined by electron energy, as different sources of energization could contribute to the precipitation of electrons of similar energy. In situ measurements can provide energy spectra that reflect particle acceleration processes in the plasma sheet, whereas radar measurements can reconstruct precipitating particle spectra that are subject to both plasma sheet and auroral acceleration processes. Using combined ground- and space-based measurements, we can distinguish different energization processes and identify source locations.

In this paper, we present observations of a substorm in the near-Earth plasma sheet with simultaneous variations in magnetic field, electron energy spectra, pitch angle distribution (PAD), and particle anisotropy in conjunction with the occurrence and motion of electron precipitation in the ionosphere. Nearly magnetically conjugate measurements were made in the ionosphere by PFISR and at the plasma sheet by the THEMIS spacecraft. The magnetic conjugacy of these measurements provides a unique opportunity to address the question of the source location and morphology of the precipitating subrelativistic electrons (>100 keV). To estimate the energy spectra of precipitating electrons, we use a maximum entropy-based inversion technique (Semeter & Kamalabadi, 2005) to "invert" altitude profiles of electron density measured at the ionosphere. This inversion technique applied to PFISR measurements provides us with quantitative estimates of precipitating electron energy spectra with a spatial and energy resolution that has been difficult to obtain previously from ground.

Here we present a quantitative comparison of different energy ranges of precipitating electrons as observed from the ionosphere and the plasma sheet. Our work reveals a close spatial and temporal correlation between the magnetic reconfiguration of the plasma sheet and the electron precipitation >10 keV observed from the ground. The energy spectrum and time variation of the 10–100 and 100–500 keV electrons broadly constrain the source region and acceleration processes within the magnetosphere that generate them. This paper demonstrates the feasibility of establishing this source partitioning using incoherent scatter radar (ISR)-based remote measurements of the *D* and *E* region ionosphere in conjunction with in situ plasma sheet measurements.

2. Experiment Overview

Clear signatures of the 10–10 and 100–500 keV populations in the high latitude ionosphere were observed during a large substorm of AE ~1400 nT at ~11:44 UT on 26 March 2008. Figure 1 illustrates the relative positions of PFISR, THEMIS All Sky Imagers, and THEMIS-D spacecraft during the growth phase (~11:15 UT) when the magnetic field configuration was tail-like. In situ measurements of PADs and magnetic fields provide insight into magnetic field topology and the spacecraft location with respect to the plasma sheet. Among the three THEMIS probes (C, D, and E) that were in the plasma sheet at most times, THEMIS-D's northern magnetic footprint estimated using the T89 magnetic field model (Tsyganenko, 1989) was at PFISR MLT at ~9:47 UT and ~1.5 hr in MLT to its west during the early expansion phase (~11:45 UT). The longitudinal extent of the substorm is much larger (~5 hr in MLT) than the longitudinal separation between the satellite footprint and PFISR. The latitudinal separation between them is ~0.5° at 9:47 UT and grows to ~4° toward the end of the substorm. This configuration offers a unique opportunity to examine transport of plasma from the plasma sheet to the ionosphere during a substorm. Convective flows in the ionosphere during this substorm were previously studied by Semeter et al. (2010).

Figure 1 depicts the type of measurement made by each instrument from ground and space and their relative positions in the magnetosphere–ionosphere system. Comparing differential electron fluxes measured by THEMIS-D ($\phi_1(E)$) and precipitating electrons estimated at the ionosphere ($\phi_2(E)$) enables us to infer the source location of particle acceleration and precipitation. $\phi_2(E)$ is estimated from the altitude profiles of PFISR electron density ($n_e(z)$) using the inversion technique described by Semeter and Kamalabadi (2005). This technique in combination with ion-chemistry models is summarized in the following subsection.

2.1. Estimating the Precipitating Electron Energy Spectrum

Precipitating charged particles cause ionization at different altitudes depending on their incident energy. Although both electrons and protons precipitate in high-latitude regions, we assume negligible contribution toward ionization from proton precipitation for altitudes <110 km because of the extreme energies required for protons to penetrate to these altitudes (Fang et al., 2013). Hence, we estimate the ion production rates due to electron precipitation from altitude profiles of electron density measured by PFISR. Alternatively, we could estimate the production rates with prior knowledge of precipitating electron energy spectra using Monte Carlo models that evaluate the effect of EEP on the neutral atmosphere (Sergienko & Ivanov, 1993). This approach constitutes a forward model, where the causal factor is the energy spectra of the precipitating electrons and the resulting observation is the altitude profile of the production rates. However, because we do not have prior knowledge of the energy spectra of precipitating electrons, we solve the inverse problem using estimated production rates from PFISR as an input to determine the precipitating electron energy spectra that caused it.

Using the principle of conservation of mass and neglecting transport processes, we estimate the production rate of electrons in the ionosphere with measured electron density as follow

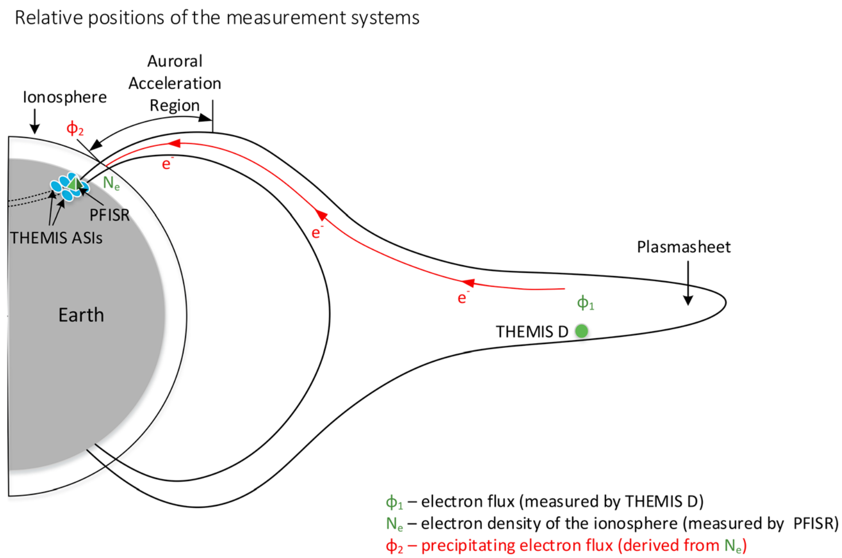

Figure 1. The relative positions of measurements and derived quantities made during the 26 March 2008 substorm. THEMIS-D is within the near-Earth plasma sheet at a distance of 7–11R_E and is also ~1R_E southward of the neutral sheet.

$$q = \frac{dN_e}{dt} + \alpha_{eff} N_e^2$$

$$N_e \sim N_i$$

Here N_e is the electron density, N_i is the ion density, and α_{eff} is the effective recombination rate. The effective recombination rate is determined by the ion chemistry in the ionosphere that varies with altitude, local time, seasons, ionization rate, and plasma density. The recombination time constants ($1/n_e\alpha_{eff}$) in the *E* and *D* regions are as low as a few seconds compared with tens of seconds in the *F* region for electron densities of ~10^{12} m^{-3} (Kirkwood & Osepian, 1995). Therefore, it is reasonable to neglect transport processes in the *E* and *D* region ionosphere as the contribution from the loss term $\alpha_{eff} N_e^2$ mostly exceeds the transport term $\nabla \cdot (n_e \vec{v})$.

The effective recombination rates in the *E* region of the ionosphere may be represented by empirical models such as those proposed by Vickrey et al. (1982). Vickrey's model assumes $\alpha_{eff} = 2.5 \times 10^{-12}\, e^{(-z/51.2)}$ [m^{3}s^{-1}], where *z* is the altitude in kilometers, which is obtained as a reasonable fit to the various profiles of effective recombination rates measured or computed by several authors for the *E* region. However, recombination in the *D* region requires a more sophisticated approach that considers the complex ion chemistry. The Sodankylä Ion Chemistry (SIC) model developed at the Sodankylä Geophysical Observatory computationally solves concentrations of several ions, negative ions, and neutral species between the altitude of 20 to 150 km, with 1 km resolution, taking into account several hundred chemical reactions and external forcing due to electron precipitation (Turunen et al., 1996; Turunen et al., 2016).

The SIC model predicts higher recombination rates at altitudes lower than 85 km as compared with the empirical model by Vickrey et al. (1982). Hence, for the same input electron density below 85 km in the *D* region, the SIC model estimates production rates that are several orders of magnitude higher than that of Vickrey et al. (1982). The SIC model is initialized by simulating only photoionization for a few days before the substorm. The model is then adapted to the PFISR measurements by searching for a production rate profile $q(z)$ that produces the observed electron density N_e. This is done independently for each altitude of the measurement and in the same time resolution as the ISR measurement. When the required $q(z)$ is found, it is smoothed and interpolated to the native altitude resolution and range of SIC and is used to obtain the production rate for the next instant of time. The model does not explicitly estimate the effective recombination rate, as it uses numerous independent reaction rates, a negative ion chemistry scheme, and ion–ion recombination coefficients to determine the electron production rates. Several studies in the past have validated the SIC model by comparing observations with the model's predictions (Verronen et al., 2005, 2015).

With a known incident energy spectrum of precipitating electrons, the forward model of the production rates computed directly using the Monte Carlo model proposed by Sergienko and Ivanov (1993) can be expressed as a system of linear equations with coefficient matrix A:

$$q = A\,\phi$$

Here A is the production rate profile per incident electron flux and is calculated by evaluating the production rate induced by a unit flux of monoenergetic electron beam precipitating into the neutral atmosphere, and ϕ is the incident differential electron number flux to the ionosphere.

With production rate q estimated from electron density measurements and the forward model A evaluated using the Sergienko and Ivanov (1993) Monte Carlo model, the differential number flux of electrons can be calculated by solving the inverse problem:

$$\phi = A^{\dagger}\,q$$

The pseudoinverse $A^{\dagger}$ is realized through the Maximum Entropy Method (Censor, 1981), a nonquadratic regularization technique. The method maximizes the Berg entropy $-\sum_{j=1}^{J}\log(\phi_j)$, and the details of the algorithm are presented in Appendix A of Semeter and Kamalabadi (2005). The inverse problem is generally ill posed. However, the Maximum Entropy Method effectively handles the ill-conditioned nature of the ISR inversion problem and preserves sharp gradients in the density during reconstruction. The inversion performs well even when a mildly underdetermined problem is posed and is insensitive to the manner in which the energy bins are distributed.

The Vickrey and SIC models estimate production rates, which are inputs to the inversion algorithm, based on the measured ionization profiles. Using the SIC model results in a higher production rate below 85 km and consequently a higher flux of precipitating electrons >50 keV, as compared with Vickrey. During quiet times, the noise power below 85 km is comparable to the signal power and calls into question the accuracy of the inferred energy spectra above 50 keV. Both models produce similar results for altitudes above 85 km and for electron energies less than 50 keV. The quality of the inversion procedure and the effect of using Vickrey and SIC model is discussed in detail in section 3.2.

In order to validate the estimated electron energy flux, a comparison between the estimate and measurements from low Earth orbit satellites is necessary. Such a comparison has been described by Semeter and Kamalabadi (2005), with FAST satellite measurements for electron energies <30 keV. The inversion procedure has also been evaluated by Zettergren et al. (2008) who used simultaneous ISR and optical spectroscopy measurements to test the internal consistency of the forward model. Currently, we do not have an independent validation of estimates of electron energies >30 keV using low Earth orbit satellites.

2.2. Instrumentation

Electron density measurements used to estimate the energy spectra of precipitating electrons in the ionosphere were made using PFISR, an electronically steerable phased-array ISR located at Poker Flat Research Range near Fairbanks, Alaska (65°N, 147.5°W). During the substorm, the phased-array system used 26 narrow beams, with a width of 1.1°, steered in a pulse-to-pulse basis within a field of view spanning from 64°N to 66°N latitude and 145°W to 149°W.

We use the THEMIS all-sky white light imagers (ASIs) to observe the evolution of the substorm from the ground. Twenty ASIs cover the higher latitudes in North America, each with a circular field of view of about 9° latitude, to ensure accurate determination of substorm onset locations to within ~1 hr of magnetic local time (Mende et al., 2008). We use three of the THEMIS ASIs situated in Gakona, Fort Yukon, and Whitehorse.

Figure 2 is a selection of mosaics of THEMIS ASIs, together with instrument locations during our event. Details of the auroral dynamics pictured in the figure is described in section 3.1. Here we note the PFISR beam configuration mapped at 110 km altitude displayed with green dots and its relative position with respect to the ASIs and magnetic footprints of the THEMIS spacecraft at the same altitude. The single beam outside the square pattern points along the local magnetic field, which is at 77.5° in elevation. A digital pulse compression technique is used, in particular a 13-baud Barker code with 10 μs bauds, for a better altitude resolution. With a pulse length of 130 μs, the altitude resolution of the measurements of electron density can be estimated to be 1.5 km. The temporal resolution of the final data product after processing the ISR

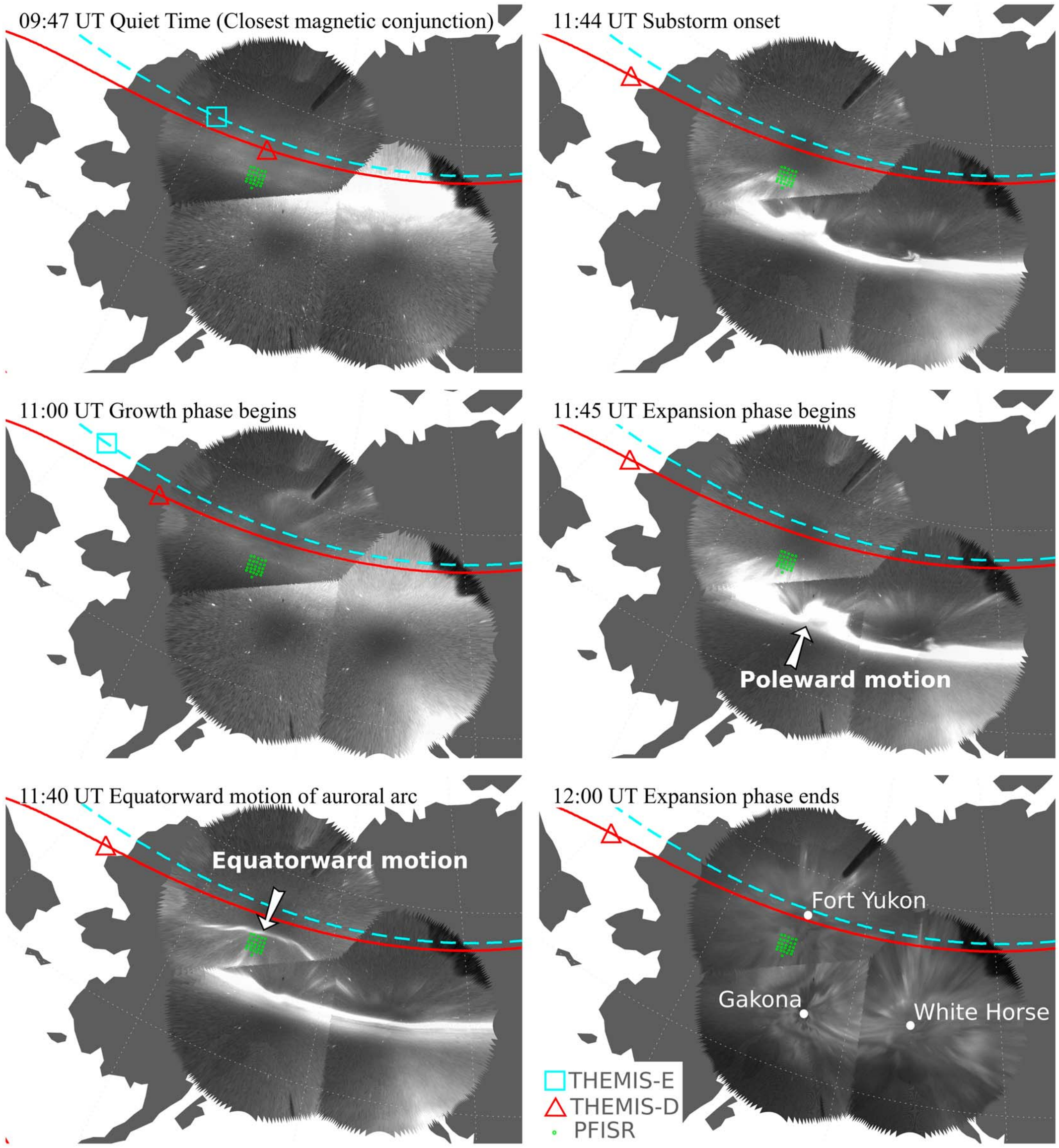

Figure 2. THEMIS all-sky image mosaics with the magnetic footprints of THEMIS-D and E along with the projection of PFISR beams, all at 110 km altitude, at different time instances during the evolution of the substorm on 26 March 2008.

spectra is 124 s. The post-processing assumes the equality of ion and electron temperatures, which is valid at lower altitudes considering the rapid energy exchange between particles through collisional processes.

We also use a suite of instruments onboard the THEMIS-D spacecraft to study the source of the precipitating electrons. We use the Electro-static Analyzer (ESA) and Solid State Telescope (SST) to measure electron energy flux from 5 eV to 1 MeV (Angelopoulos, 2008). These instruments can also measure the PAD of electron and ions with an angular resolution of 22.5°. The SST and ESA Level-2 data products are calibrated and have undergone improvements to mitigate contamination. We use the latest calibrated and corrected data uploaded on January 2014 with a temporal resolution of 96 s. The Fluxgate Magnetometer (FGM) onboard THEMIS produces vector magnetic field measurements of the background DC magnetic fields with a 3 pT resolution and ±25,000 nT range (Auster et al., 2008), which can be used to study the reconfigurations in the Earth's magnetosphere during the substorm. We also use the FGM measurements to estimate wave power along the GSM-X axis for frequencies below 1 Hz. The Electric Field Instrument (Bonnell et al., 2009), which has a sensitivity of 10^{-4} mV/m$\sqrt{\mathrm{Hz}}$ at 10 Hz, was used simultaneously to estimate wave power along the GSM-Y axis for the same frequencies. The Search Coil Magnetometers can make measurements between

0.1 Hz and 4 kHz with sensitivities of 0.8 $\mathrm{pT}/\sqrt{\mathrm{Hz}}$ at 10 Hz and 0.02 $\mathrm{pT}/\sqrt{\mathrm{Hz}}$ at 1,000 Hz (Roux et al., 2008). We use the Search Coil Magnetometers data to estimate wave power for frequencies between 1 and 1,000 Hz.

3. Observation

In this section, we describe measurements made by the THEMIS ASIs, THEMIS spacecraft, and PFISR along with estimates of precipitating electron spectra made by inverting measured electron densities during the substorm event on 26 March 2008.

3.1. Substorm Overview

In the first snapshot of Figure 2 at 9:47 UT, the sky within the PFISR field of view is relatively quiet and dominated by diffuse aurora as the preceding substorm concludes. At this time, the THEMIS-D magnetic footprint is closest to PFISR. From about 11:00 UT, the diffuse aurora starts to move equatorward signaling the beginning of the growth phase. A few discrete arcs are also observed moving equatorward during the growth phase. Note a bright one at 11:40 UT moving equatorward through the PFISR field of view. A sudden brightening of the equatorward arc occurs at ~11:44 UT and continues to increase in intensity followed by poleward expansion from 11:45 UT, signaling the onset and expansion phase of the substorm. The expansion phase lasts until about 12:00 UT, after which the aurora starts to become fainter—indicating a transition into the recovery phase that ends at about 12:30 UT after which the intensity and activity in the night sky returns to what was observed before the growth phase.

Figure 3 presents a global perspective of the substorm using both space- and ground-based measurements. Figure 3a shows the interplanetary magnetic field (IMF) along the GSM-Z axis measured by the ACE satellite and time-shifted to the bow shock nose. At 10:40 UT, the IMF turns southward, which presumably created conditions for reconnection in the dayside and hence initiating the growth phase of the substorm at ~11 UT. Around this time in Figure 3b, the keogram from Fort Yukon (FKYN) THEMIS ASI located at 66.56°N–145.21°E close to Poker Flat clearly shows a decaying diffuse aurora. From about 11:00 UT, the auroral intensities move equatorward as seen in the keogram from FYKN and also Gakona (GAKO) THEMIS ASI located equatorward of PFISR at 63.05°N–145.16°E (Figure 3c). The AL index in Figure 3d and the earthward component of the magnetic field (B_x) measured by THEMIS-D in Figure 3e decrease (or increase in magnitude), suggesting formation of ionospheric currents and tail-like magnetospheric configuration. Figure 3f is an altitude profile of the electron density obtained by spatially averaging across all 26 beams of PFISR, also making the assumption that the ion and electron temperatures are the same throughout. The averaging allows for better statistics while limiting the spatial resolution to about ~0.5° in magnetic latitude. For altitudes less than 85 km, the electron density observed is typically below 10^{10} m^{-3}, and they have comparatively poor signal-to-noise ratio. As the diffuse aurora crosses the PFISR field of view, we observe substantial *D* region ionization in Figure 3f between 11:00 and 11:30 UT, suggesting a hardening of the precipitating electron energy spectra. However, in Figure 3g, we observe a softening of the THEMIS-D electron energy spectra during this period. The apparent disparate behavior of the energy spectra of plasma sheet and precipitating electrons during this period, probably because of the longitudinal and latitudinal separation between THEMIS-D magnetic footprint and PFISR, is discussed further in section 4. There is beam-to-beam variation observed during this period that may contribute in part to the lack of correlation with plasma sheet electrons. However, the spatial averaging across beams is more valid during the expansion phase and before the growth phase as there are no significant beam-to-beam variations.

Toward the end of the growth phase ~11:37 UT, we see signatures of a pseudo-breakup from GAKO ASI keogram. Following this at ~11:44 UT, B_x and B_z start to increase rapidly, signaling dipolarization. This coincides with a further auroral brightening, followed by poleward expansion and thus the substorm onset. Based on the white light images measured by THEMIS ASIs displayed in Figure 2, the onset location was identified to be westward of Poker Flat. During the expansion phase, enhanced ionization is observed by PFISR over altitudes as low as 70 km (Figure 3f), indicating enhanced precipitation of electrons with energies greater than 100 keV. The expansion phase of the substorm continues up to 12:00 UT, where the AL index reaches its peak value, and the substantial low-altitude ionization continues to be observed by PFISR. From 12:00 UT, the recovery phase begins with the AL index and auroral intensities at FYKN gradually returning back to the pre-substorm configuration at about 12:30 UT.

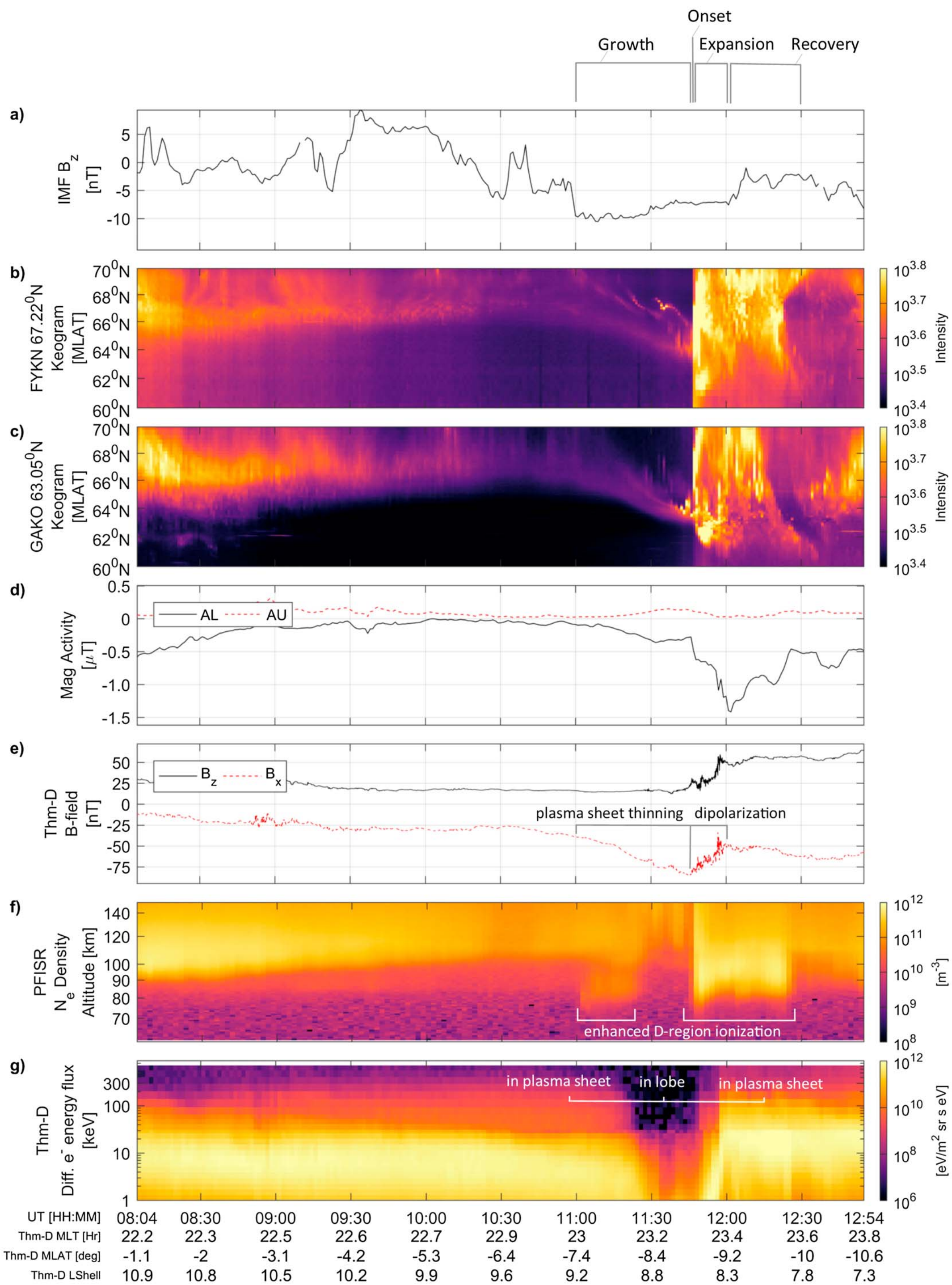

Figure 3. Overview of relevant ground- and space-based measurements during the substorm on 26 March 2008: (a) Northward IMF component from ACE spacecraft time-shifted to the bow shock nose; (b) optical keogram from an ASI at Fort Yukon; (c) same from Gakona; (d) auroral electrojet indexes AL and AU; (e) measurements of *z* and *x* components of the DC magnetic field in GSM coordinates from THEMIS-D; (f) altitude profiles of electron density by PFISR (averaged across 26 beams); and (g) differential energy flux of electrons from THEMIS-D.

During the expansion phase, sharp increase in electron energy flux greater than 100 keV was also observed by the THEMIS-D spacecraft. Figure 3g shows the time series energy spectra of electrons of ~1 to 1,000 keV in the plasma sheet, developed by combining energy spectra measurements from ESA (electrons <25 keV) and SST (electrons >25 keV) onboard the THEMIS-D spacecraft. The energy spectra observed by THEMIS-D

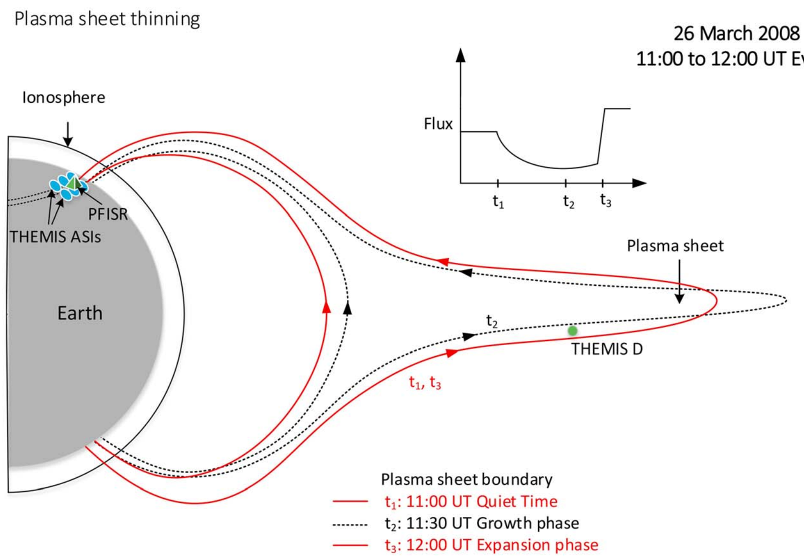

Figure 4. Diagram of plasma sheet thinning and expanding before and after the substorm onset. At time t_1 before the growth phase, the plasma sheet extends up to about $5R_E$ from the neutral sheet. This phase is not represented in the diagram. However, after t_1, during the growth phase, the plasma sheet starts thinning, and the spacecraft THEMIS-D finds itself in the lobe region by t_2. At t_3, the substorm onset causes rapid expansion of the plasma sheet, because of dipolarization of the magnetic field, and the spacecraft suddenly finds itself within the central plasma sheet with an increased energetic electron flux.

between 11:00 to 11:44 UT is characteristic of plasma sheet thinning known to occur during the growth phase (Pytte & West, 1978). As the plasma sheet thins, the plasma sheet boundary layer passes through the spacecraft, and the spacecraft finds itself in the magnetospheric lobe region after 11:30 UT, where the density of electrons is very low. The satellite's position relative to the plasma sheet during different phases of the substorm is described in Figure 4. From 11:44 to 11:55 UT during the expansion phase, the satellite re-enters the plasma sheet as the tail undergoes dipolarization and the plasma sheet expands, and the measured energy flux is much higher than before the onset.

3.2. Inversion Results

In Figure 5, we compare the time series differential energy flux of precipitating electrons in the ionosphere with that measured by THEMIS-D in the plasma sheet. Figure 5a,b shows the results of the inversion carried out using the Vickrey and SIC models, respectively. They provide a comparison of the inversion technique carried out by two different ion-chemistry models, which resulted in similar energy fluxes for energies less than 100 keV. Figure 5c, which is the same as Figure 3g, shows the differential energy flux of plasma sheet electrons measured by THEMIS-D. It is repeated here to highlight the temporal correlation observed between the energy spectra estimated in the ionosphere and the plasma sheet. The THEMIS-D spacecraft measures the trapped particle population, as it is located close to the magnetic equator and is within the plasma sheet, where the loss cone is less than the angular resolution of the particle detector. However, by definition, PFISR measures particles within the loss cone as they precipitate into the ionosphere. The population of electrons greater than a few tens of kilo-electron volts is mostly higher in THEMIS-D measurements than in PFISR, as indicated by the difference in the energy spectra between the trapped particles and loss cone particles (Figure 5c). Figure 5a–c shows at least an order of magnitude increase in the net energy flux across all energies after the onset at 11:44 UT as compared with the growth phase. Between 11:00 and 11:30 UT in Figure 5a,b, we observe energy flux enhancements of ~70–100 keV electrons associated with the enhanced *D* region ionization mentioned in the previous section. This enhancement is not observed in the THEMIS-D energy spectra (Figure 5c) because of a lesser degree of magnetic conjugacy during growth phase.

Figure 5d,f shows the corresponding cumulative energy flux distribution of the differential energy flux in Figure 5a–c, normalized to the highest total energy flux estimated in the time span of the corresponding result. The color indicates the percentage of energy flux of electrons below a particular energy, relative to the highest total energy flux observed within the time span. The median energy of the energy spectra is represented with a cyan line in Figure 5d,f. During the growth phase at PFISR from 11:00 to 11:44 UT, the

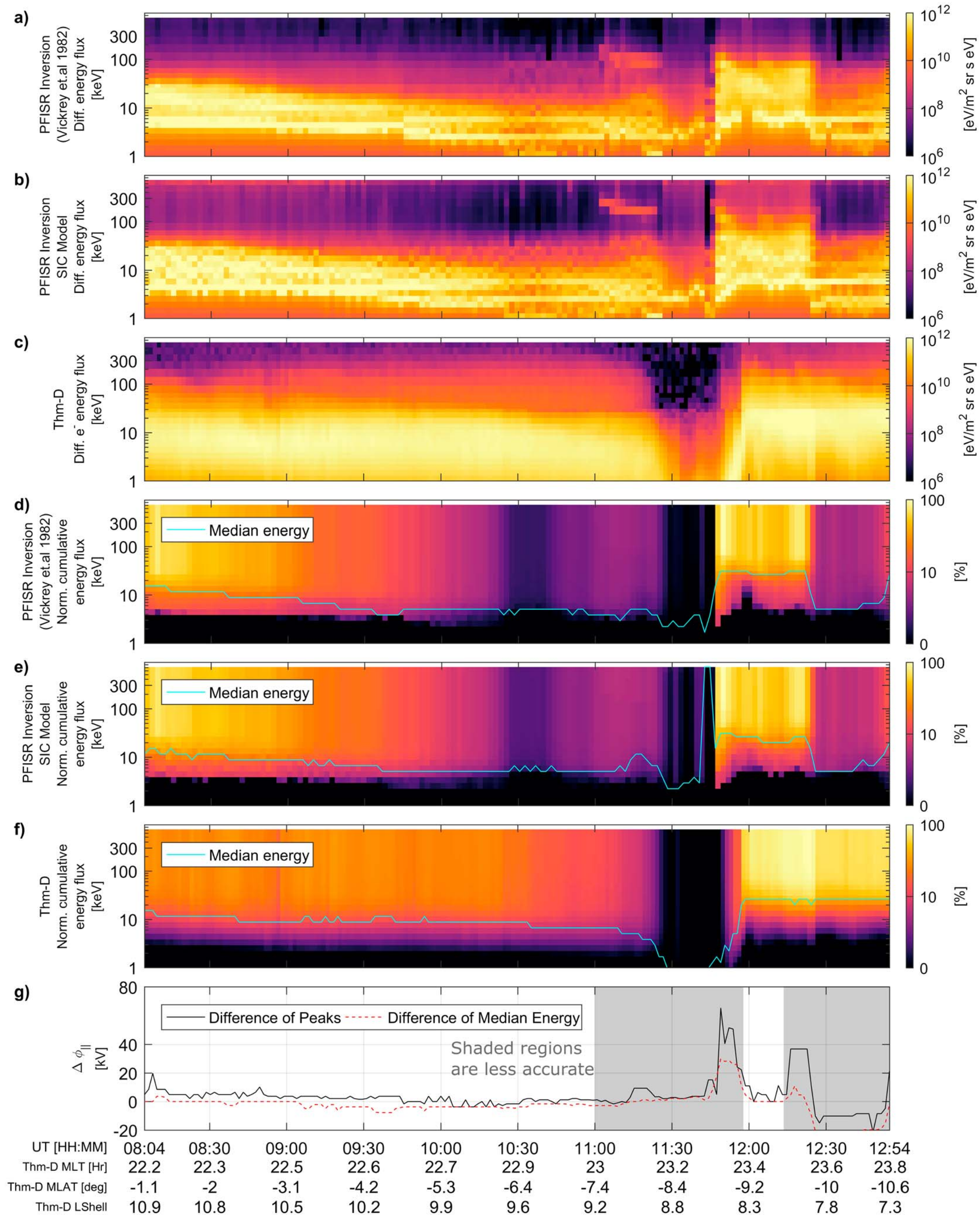

Figure 5. Inversion results of PFISR electron density measurement in comparison with THEMIS-D energy spectra: (a–c) Differential electron energy spectra estimated from PFISR measurements using Vickrey model, the same using SIC model, and measured using THEMIS-D, respectively; (d, f) normalized cumulative energy spectra of the same; and (g) maximum potential drop estimated from the differences in peak and median energy in the differential electron energy spectra between PFISR and THEMIS-D.

distribution has a median energy value of 5 keV, which increases to 30 keV after the onset (Figure 5d,e). This is roughly consistent with THEMIS-D measurements in the plasma sheet with a 7 keV median for the electron energy spectra during the growth phase and 25 keV after the onset (Figure 5f).

Note the qualitative agreement between the differential energy flux in Figure 5a–c and normalized cumulative energy flux in Figure 5d,f. Comparing the differences in the energy distributions in the plasma sheet and the ionosphere, we can estimate the maximum parallel potential required to accelerate the loss cone electrons. Figure 5g displays the maximum parallel potential between the plasma sheet and the ionosphere estimated from the differences in the high-energy peaks (black solid line) and the median energy (red dashed line) of the loss cone energy spectra. In reality, the parallel potential drop is likely to be less than this value because of simultaneous pitch angle diffusion effects that may affect the median energy or high-energy peaks. Before the substorm onset, the estimated parallel potential drop is a few kilovolts. After the onset, it is as high as ~10–20 kV, indicating an active AAR. However, beyond 11:00 UT, the estimate has a lot of uncertainty as longitudinal separation between THEMIS-D and PFISR increases substantially even though latitudinal variability remains small. Because of this separation, the spacecraft is within the magnetic lobes during 11:44 to 11:55 UT and sees little or no electron flux at higher energies, leading us to inaccurately estimate a higher potential drop (~70 kV) between the plasma sheet and the ionosphere. Between 11:55 and 12:15 UT, the satellite finds itself moving into the plasma sheet and observes the same population as observed by PFISR—estimating ~10–20 kV potential difference. At about 12:20 UT, the potential difference estimated from energy peak differences reaches about 35 kV, probably because of enhanced precipitation of subrelativistic electrons associated with diffuse aurora observed toward the end of the expansion phase rather than increased parallel electric fields. Time spans with less reliable estimates have been shaded grey. Although the shaded region spans most of the time of interest, the panel demonstrates that a time series estimate of parallel potential difference between the plasma sheet and the ionosphere can be developed with magnetically conjugate energy spectra measurements from ISR and spacecraft.

Figure 6 demonstrates the validity of the techniques presented in this paper by comparing measured data with the estimates derived using the inversion procedure and the ion-chemistry models. It compares the electron density, production rate, and energy spectra estimated by PFISR using Vickrey and SIC Models with those estimated and measured by the THEMIS-D spacecraft. The top panels display data at 9:47 UT, when the THEMIS-D magnetic footprint at 110 km is closest to PFISR field of view projected at 110 km. The bottom panels display data during the expansion phase at 11:46 UT, when the energy flux of electrons is high in the ionosphere but not yet in the plasma sheet because of the longitudinal separation of the spacecraft from PFISR. As mentioned earlier, the substorm onset occurs close to Poker Flat. However, the spacecraft at this time is longitudinally separated by ~1.5 MLT from Poker Flat and hence finds itself farther from the substorm dipolarization front that grows at a rate less than the Alfven speed. As a result, THEMIS-D is at the outer boundary of the plasma sheet and measures a lower energy flux of electrons at the time. However, we expect the energy spectra of plasma sheet electrons observed by the satellite and PFISR to be broadly correlated, as the longitudinal separation of the spacecraft footprint from Poker Flat is well within the substorm's spatial extent.

Figure 6a,b displays the electron density directly measured by PFISR (solid black line) and the uncertainty in the ISR electron density measurements σ_{N_e}(dashed black line). The dashed magenta line is the forward modeling of the inverted electron flux estimated using Vickrey model, which when compared with the electron density directly measured by PFISR indicates the quality of the inversion technique. The dotted blue line is the forward modeling of the THEMIS-D measurement, also using the Vickrey model of effective recombination rates. Comparing this with the PFISR electron density measurement, we can evaluate the degree to which the ionization caused by precipitating loss cone electrons resembles the ionization that may be caused by the precipitation of the entire electron population in the plasma sheet measured by the spacecraft.

Figure 6c,d displays data that go through similar processing as that in Figure 6a,b, except that they display the production rates derived from the PFISR measurements using Vickrey (black solid line) and SIC models (red solid line). The uncertainty in terms of the production rate, σ_q (black dashed line), is derived by differentiating $q = \alpha_{\mathrm{eff}}\, N_e^2$ so that $\sigma_q = 2\alpha_{\mathrm{eff}} N_e \sigma_{Ne}$. It is propagated through the Vickrey model and results in an order of magnitude or more uncertainty in the production rate derived from PFISR measurements below ~85–95 km altitude at 09:47 UT and below ~70 km altitude at 11:46 UT. The altitudinal variability is high below ~85 km at 09:47 UT and ~70 km at 11:46 UT. The same is true for the measured electron density in Figure 6a,b. In Figure 6a, between 85 km and 95 km, the uncertainty only becomes comparable to the signal at a few points. The ISR measurement uncertainty causes the production rates estimated by the SIC model to increase substantially and abruptly below 85 km altitude at 09:47 UT and below 70 km altitude at 11:46 UT. Thus, this increase cannot be considered a result of primary electron precipitation. These altitudes correspond to peak production rates caused by 100 keV at 09:47 UT and ~400 keV at 11:46 UT. Because of low

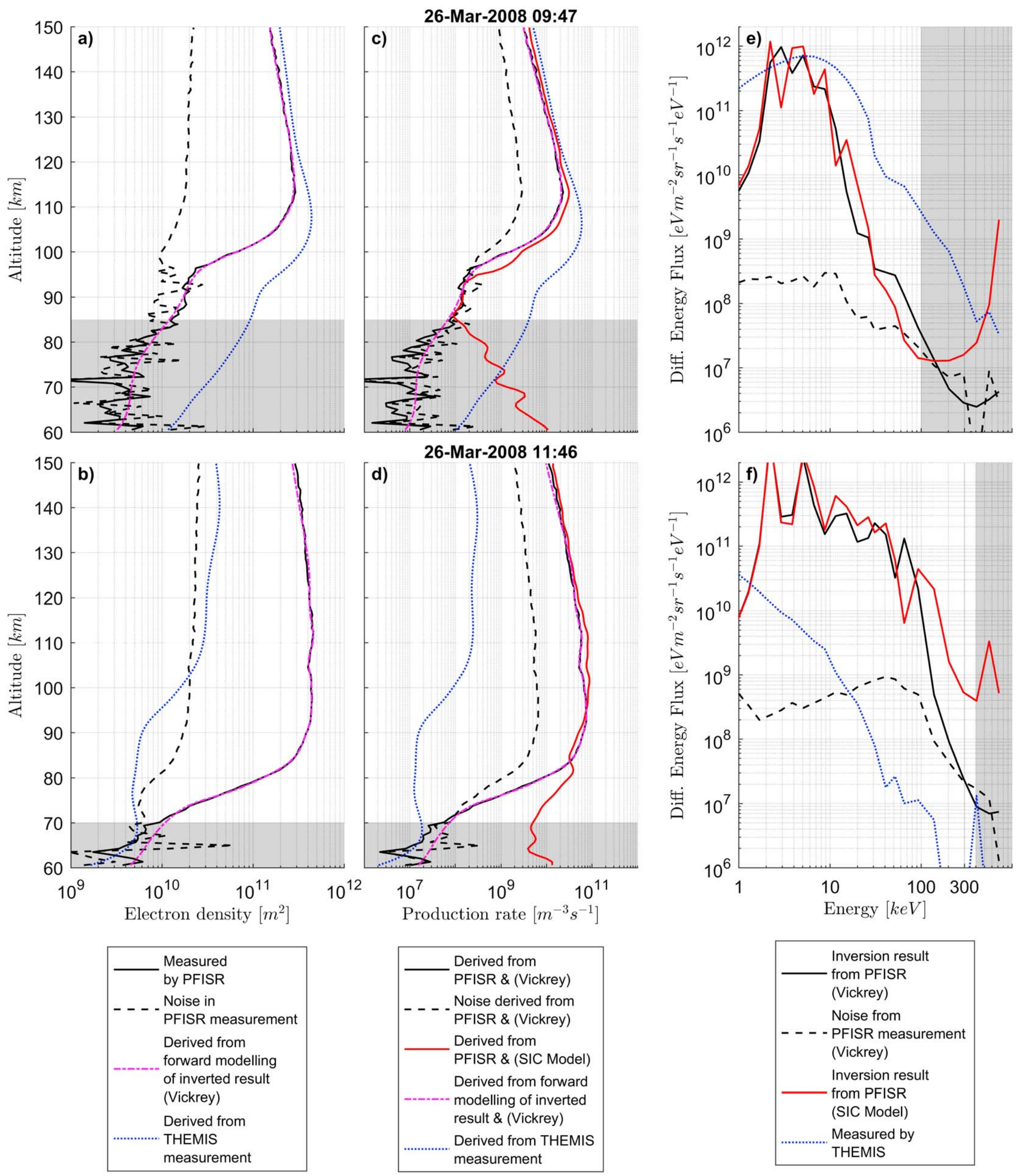

Figure 6. Electron density, production rate, and differential energy spectrum estimates from PFISR and THEMIS-D measurements contrasted against each other at two time instances 9:47 UT and 11:46 UT. THEMIS-D's magnetic footprint was closest to PFISR at 9:47 UT, and the highest auroral intensities after the substorm onset was observed at 11:46 UT. The shaded areas have poor signal-to-noise ratio.

signal to noise ratio and large variability in density with altitude, we consider the regions of the plot that are shaded grey as unreliable.

Figure 6e,f shows the results of the inversion process in the form of differential energy flux. The black solid line represents the inversion result from PFISR measurements estimated using the Vickrey model, whereas the black dotted line represents the estimated noise in the energy flux using the same model, and the red solid line represents the inversion result estimated using the SIC model. The error in energy flux is estimated using the diagonalized covariance matrix C_ϕ, where $C_\phi^{-1} = A^T C_q^{-1} A + [\text{Diag}(\Gamma\phi)]^{-1}$ (Hysell, 2007). We compare all of these with the closest magnetically conjugate measurement of differential energy flux made by THEMIS-D spacecraft. In Figure 6f, we observe that the energy flux of electrons in the ionosphere greater than 10 keV increases by several orders of magnitude at 11:46 UT, compared with the energy flux before the substorm. It is also important to note that the Vickrey and SIC models predict almost the same production

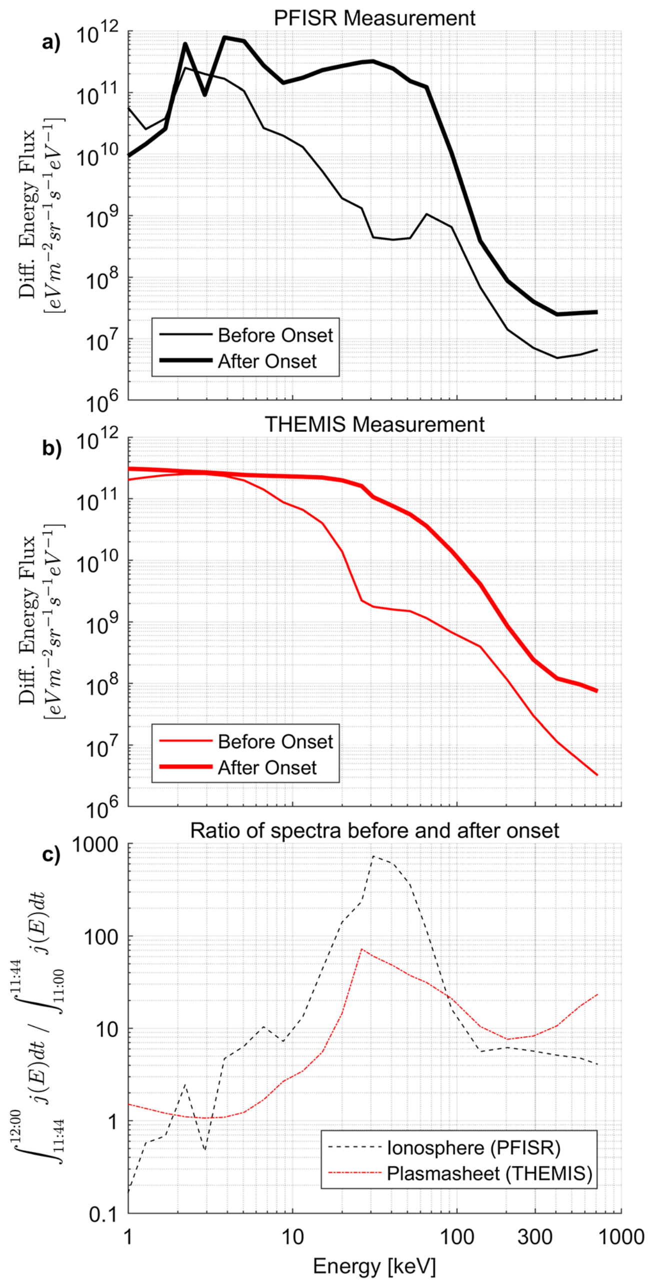

Figure 7. Time-averaged energy spectra during (a) the growth phase of the substorm (11:00 UT to 11:44 UT), (b) the expansion phase of the substorm (11:44 UT to 12:00 UT), and (c) their ratio.

rates and differential energy flux above 85 km (below 100 keV), respectively. However, between 70 and 80 km in Figure 6d, the SIC model predicts 1–2 orders of magnitude higher production rates and consequently predicts a higher precipitating energy flux for energies >100 keV as compared with the Vickrey model in Figure 6f.

Figure 7a,b shows the time-averaged electron energy spectra before and after the substorm onset, both in the ionosphere and the plasma sheet, respectively. These panels present the effect of acceleration processes during the substorm on the electron energy spectra measured in the ionosphere and the plasma sheet. The spectra before onset are averaged across 11:00 to 11:44 UT and after onset are averaged across the period 11:44–12:00 UT. Apart from the peak observed at around 2–5 keV before the onset, corresponding to the energy range of visible auroral precipitation, a secondary peak at about 70 keV with lower flux is observed during growth phase. However, after the onset, during the expansion phase, the peak shifts to about 30 keV, with a precipitating high-energy tail that extends higher than 100 keV. Figure 7c shows the ratio of the time-averaged energy spectra before and after the onset in the ionosphere and the plasma sheet. This panel compares the changes in the time-averaged energy spectra due to the onset in the ionosphere and plasma sheet. For energies between 2–5 and ≳100 keV, the ratio of the energy flux before and after the onset remains within an order of magnitude in the ionosphere and the plasma sheet. However, for energies between ~4 and 60 keV, the ratio is nearly an order of magnitude higher in the ionosphere compared with that measured in the plasma sheet.

Figure 8a,b shows the normalized cumulative energy spectra before and after the onset in the ionosphere and plasma sheet, respectively, averaged across the same period mentioned above. These panels provide an estimate of the proportion of energy within different electron energy ranges before and after the onset. The dashed lines represent the median energy flux value and can be used to find the corresponding median energy. The median energy increases from about 3 to 30 keV in the precipitating electron flux within the ionosphere and from about 5 to 20 keV in the plasma sheet. The total time-averaged energy flux increase measured after the substorm onset is about 20 times in the ionosphere and five times in the plasma sheet, suggesting a substantial increase in the loss cone population. The proportion of energy flux contributed by 10–100 keV electrons increased from less than 15% of the total energy flux before the substorm onset to about 75% after the onset.

3.3. Pitch-Angle Anisotropy and Wave Power

To identify possible mechanisms of enhanced precipitation of ~100 keV electrons, we examine pitch angle anisotropy and wave power at THEMIS-D. Figure 9a,b displays the ion and electron pitch angle anisotropy $\left(A = \frac{V_\perp}{V_\parallel} - 1\right)$ calculated from the PAD obtained from THEMIS-D ESA and SST instruments through the duration of the substorm. An anisotropy value of A~0 implies the particles have almost equal perpendicular and parallel energy and hence have an isotropic distribution. $A > 0$ implies greater perpendicular energy or a pancake-type PAD. $A < 0$ implies greater parallel energy or a field-aligned PAD. For electrons greater than 30 keV, from 8:00 to 11:00 UT we observe a bidirectional and field-aligned PAD, characteristic of the plasma sheet boundary layer (PSBL; Parks et al., 1984). At 11:03 UT, the probe is in the outer edge of the PSBL, where the energy flux starts to drop, and the electron PAD is isotropic. Up to 11:44 UT, the flux is too low to determine the nature of the PAD. Immediately after 11:44 UT, the probe finds itself moving through the PSBL into

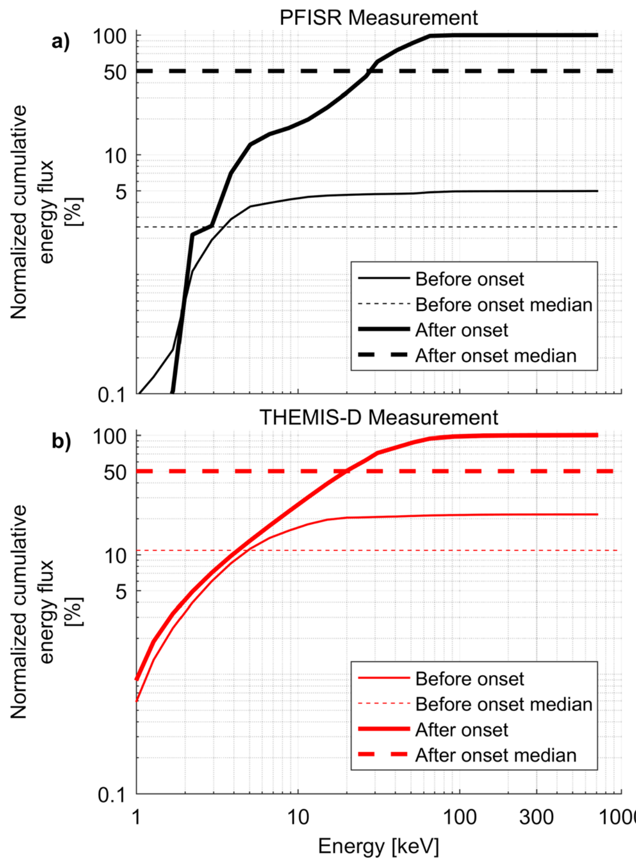

Figure 8. Normalized cumulative energy spectra (in percentages) during the growth phase (11:00–11:44 UT) and expansion phase (11:44–12:00 UT) of the substorm estimated from (a) PFISR measurement and (b) THEMIS-D measurement.

the central plasma sheet, where the distribution is isotropic—as the particles scatter off the neutral sheet (Pytte & West, 1978). After several minutes, the PAD settles down to a pancake-type distribution, with lower flux at pitch angles outside 70–110°.

The energetic ions >25 keV show a positive anisotropy, during the growth phase, and become more isotropic as the expansion phase proceeds. A positive ion anisotropy can lead to generation of electromagnetic ion cyclotron (EMIC) waves. Figure 9c,e displays the power spectra of high frequency waves (1–1,000 Hz) and low frequency waves (1–1,000 mHz) along the GSM-X and GSM-Y axes. Figure 9e also displays the ion cyclotron frequencies of the major ions present in the plasma sheet. EMIC waves may account for enhanced wave power below ion cyclotron frequencies displayed in Figure 9d,e. The minimum cyclotron resonance energies are low enough for electrons to be scattered by EMIC waves with the upper cutoff frequency (ω_{UC}) estimated using the ion densities measured in the plasma sheet (Albert, 2003). The observed wave frequencies are also high enough to meet the minimum resonant energy condition. The EMIC wave amplitudes are enhanced substantially during the substorm expansion between 11:46 UT and 12:30 UT, increasing their efficiency in scattering electrons with subrelativistic energies or higher. Figure 9c also shows signs of possible chorus waves close to the substorm onset time.

4. Discussion

4.1. Correlation in the Energy Spectra

As IMF turns southward at 10:40 UT (Figure 3a), the favorable conditions for dayside reconnections cause magnetic fluxes of open field lines to increase in the tail lobes, accompanied by an increase in the earthward component of the tail magnetic field, B_x (Figure 3e), during the growth phase. This is causally linked to the thinning of the plasma sheet as observed by THEMIS and the simultaneous equatorward motion of the auroral oval crossing the field of view of PFISR. We observe temporally correlated decrease in the electron energy fluxes up until 11:44 UT (Figure 5a–c) as THEMIS-D and PFISR are nearly magnetically conjugate. However, the transport of magnetic flux and frozen in particles associated with the plasma sheet thinning causes this decrease in energy flux. As the plasma sheet thins down, the spacecraft finds itself moving toward the outer boundary of the plasma sheet as described in Figure 4. Measurements of PADs from THEMIS further support this conclusion.

The bidirectional and field-aligned PAD of electrons >30 keV observed before the growth phase (Figure 9b from 9:45 to 11:00 UT) is characteristic of the energetic electrons drifting into the nighttime magnetosphere while the field is more or less in a dipole configuration (Pytte & West, 1978). From 11:00 to 11:44 UT during the growth phase of the substorm (see Figure 3a), the AL index increases to very high magnitudes from −285 to −1403 nT, signaling the shunting of the cross-tail currents through the ionosphere typical of the substorm onset (Baker et al., 1996). Closer to the outer boundary of the PSBL at about 11:03 UT, the PAD of electrons >30 keV immediately transitions to an isotropic distribution. These isotropic distributions are typically observed when electrons encounter a more tail-like magnetic field configuration, and the first and second adiabatic invariants break down because of the large electron gyroradius ρ in the vicinity of the neutral sheet crossing in comparison to the field curvature R_c $\left(\frac{\rho}{R_c} \gtrsim \frac{1}{10}\right)$ (Alfvén & Fälthammar, 1963). Between 11:20 UT to 11:50 UT in Figure 3g, we observe extremely low flux at higher energies (characteristic of the magnetic lobe) and consequently an erratic PAD because of the low number of samples. Because of their near magnetic conjugacy, the effect of the outer layer of the plasma sheet boundary crossing THEMIS and PFISR was observed almost simultaneously by both as the plasma sheet thins down and the foot of the outer boundary of the plasma sheet in the ionosphere moves equatorward till about 11:44 UT. We speculate that the secondary peak of ~70 keV electrons observed at the ionosphere in the early part of the growth phase ~11:00–11:30

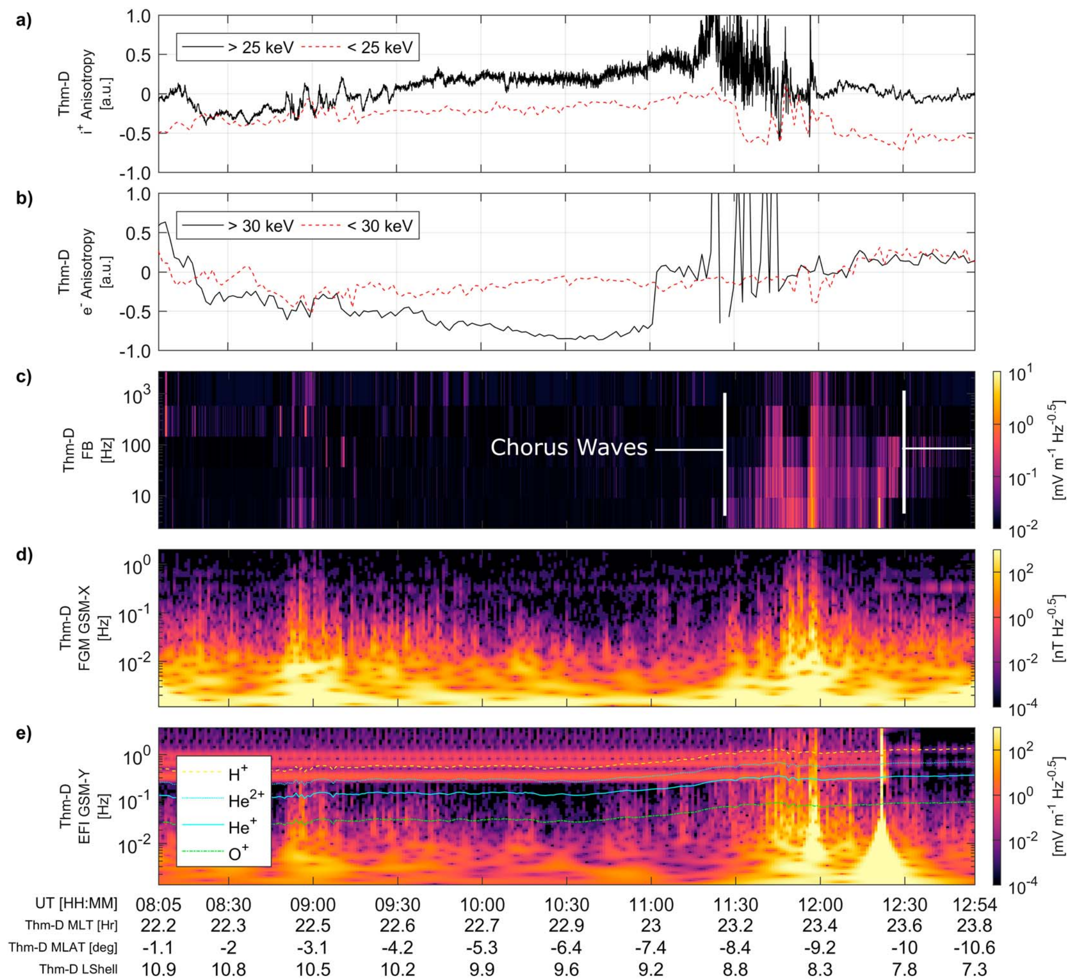

Figure 9. Particle anisotropy and wave energy measured by THEMIS-D during the 26 March 2008 substorm: (a) Ion anisotropy and (b) electron anisotropy measured at the plasma sheet; (c) power spectra of high-frequency waves from THEMIS-D filter bank measurements; (d) power spectra along GSM-X axis of low-frequency waves from THEMIS-D FGM measurements; and (e) the same along GSM-Y axis from THEMIS-D EFI measurements overlaid with estimated local ion gyrofrequencies.

UT (see Figure 7a) may be caused by precipitation from the equatorward-moving trapping boundary, located between the outer-radiation belt and the plasma sheet (Kirkwood & Eliasson, 1990). The outer boundary of the plasma sheet moves across the spacecraft at ~11:55 UT, bringing with it a high intensity of isotropic/pancake PADs characteristic of the inner plasma sheet during the expansion phase (Parks et al., 1984). This increase in intensity was a result of dipolarization and was delayed by about 11 min with respect to PFISR observations of the poleward boundary swiftly moving northward across the ionosphere at the substorm onset (~11:44 UT). This delay is due to the MLT difference between the THEMIS footprint and PFISR.

4.2. Source Location of Energetic Particles

In this section, we use the following arguments to gauge the source location of the precipitating particles and qualitatively identify the contribution of pitch angle scattering and energization processes affecting them. A correlated variation in the energy spectra at two magnetically conjugate locations, being on opposite sides of the magnetic equatorial plane, suggests that processes between these two locations caused no variations in the pitch angle distribution. It also suggests that the source of these particles lies tailward of the measurement location closest to the magnetic equator. A shift in the median or peak energy in the energy spectra between the two magnetically conjugate locations suggests energization processes acting between the two locations. An uncorrelated variation in the energy spectra without any clear change in the median or peak energy indicates processes that cause pitch angle diffusion between the two magnetically conjugate locations.

In Figure 7c, the time-averaged energy flux of electrons $>$100 keV within the plasma sheet increases up to about five to eight times after the onset whereas that of electrons around 30 keV increases up to 60 times. However, the time-averaged energy flux of low energy electrons of about 3 keV does not change much. The same trend is more or less reflected in the ionosphere, with the exception that the increase in precipitated electron energy flux for ~30 keV electrons is about 700 times that before the onset. This uncorrelated increase in energy flux for 10–100 keV electrons precipitating in the ionosphere suggests pitch angle scattering due to processes in the AAR or tailward. We estimate the parallel potential drop (Figure 5g) by calculating the difference in median and peak energies between the loss cone electrons in the ionosphere and the plasma sheet. Figure 5g confirms the increase in parallel potential drop after the onset with a maximum of ~10 kV, suggesting energization of cold electrons by the AAR to ~10 keV. The increase in the energy flux of subrelativistic electrons $>$100 keV seen in Figure 7c at both the ionosphere and plasma sheet suggests the location of the source of these electrons to be at or tailward of ~9R_E. Figure 8 shows the normalized cumulative energy spectra, time-averaged during the growth phase (thin line) and the expansion phase (thicker line), which can be used to estimate the percentage of energy flux up to a particular energy value. We observe a considerable hardening of the spectra after the substorm onset, with an increase in median energy of ~15 keV in the plasma sheet and ~25 keV in the ionosphere compared with that before the onset.

4.3. Substorm Motion

The time difference of enhanced particle flux in the beginning of the expansion phase observed by PFISR and THEMIS-D is about 11 min (~11:44 UT at PFISR and ~11:55 UT at THEMIS-D). THEMIS-D's magnetic footprint is at 68°N, 169.3°W, which is about 22° westward of PFISR. Moreover, THEMIS-E and THEMIS-C are also within the plasma sheet during our period of interest, and further westward of THEMIS-D, they measure the arrival time to be ~12:00 UT and ~12:30 UT, respectively. The westward delay in arrival of the energetic particles suggests that the substorm onset is located at an MLT very close to Poker Flat and expands westward. The substorm also expands eastward, to a lesser degree from Poker Flat. Evidence for this can be seen in Figure 2, which shows intense auroral brightening at ~11:44 UT longitudinally close to Poker Flat expanding eastward in ~11:45 UT.

4.4. Distribution of Energetic Electrons Within the Plasma Sheet and Corresponding Auroral Arc

The outer boundary of the plasma sheet is assumed to map down to the poleward region of the diffuse auroral arc (Lui et al., 1977). During the growth phase, THEMIS ASIs observe equatorward motion of the arc in the ionosphere, whereas both PFISR and THEMIS observe precipitating electron population from the inner to the outer boundary of the plasma sheet. At 11:00–11:10 UT, the outer boundary of the plasma sheet moves across THEMIS, and the poleward edge of the auroral arc moves equatorward across PFISR's field of view. During this period, Figure 5a–c shows the flux of energetic electrons to be decreasing rapidly 1–2 min earlier than the flux of the lower energy electrons in both the ionosphere and the plasma sheet. This observation suggests that the inner edge of the plasma sheet boundary layer has a harder spectrum as compared with the outer edge, and similarly, the equatorward edge of the poleward boundary of the auroral arc has a harder spectrum than the poleward edge. The median energy of precipitating electrons in the equatorward edge is ~5 keV, which reduces to ~3 keV in the poleward edge. A pair of example spectra is included as supporting information (Figure S1).

4.5. Pitch Angle Anisotropy

The pitch angle anisotropy of a particle distribution, defined as $A = \frac{W_\perp}{W_\parallel} - 1$, is a useful indicator of wave growth. A sufficiently positive anisotropy of the electron or ion pitch angle distribution can cause growth of either the whistler mode or ion cyclotron mode. The anisotropy also gives clues to the type of acceleration or scattering mechanism that is acting on the distribution. Processes that act along the field-aligned direction like Fermi acceleration, field aligned potential drops, Alfven waves, or Speiser motion (Wang et al., 2013) are likely to cause negative anisotropy, whereas processes like betatron acceleration cause an increase in the perpendicular energy resulting in a positive anisotropy. Fermi acceleration of the kind described in Ganguli et al. (1995) can cause acceleration during the growth phase along the cross-tail electric field, leading to positive anisotropy. The highly bidirectional pitch angle distribution of the high energy electrons is likely caused by Fermi acceleration during plasma sheet thinning (Hada et al., 1981).

4.6. Wave Scattering and Energization

An analysis of the wave power measured by THEMIS-D confirms the presence of EMIC waves during the growth phase, produced probably due to the positive anisotropy of high-energy ions. EMIC wave interactions with electrons have been proposed to account for the bursty precipitation following substorms by Lorentzen et al. (2000). An estimate of the minimum kinetic energy needed by the electron for cyclotron resonance with the EMIC wave produced by different ion species, made using equation 19 from Albert (2003), is included as supporting information (Figure S2). Up to two orders of magnitude increase in the wave power is observed at almost all frequencies from growth phase (~10:40 UT) to expansion phase (11:51 UT), suggesting a possible increase in pitch angle scattering of electrons $>$100 keV due to EMIC waves produced by H^+ or O^+ ions. O^+ ion concentrations are higher during substorms (Lennartsson, 1987), reaching proportions up to about 20%, thereby increasing the probability of electron scattering. An additional mechanism for scattering could be bounce resonance with EMIC waves, which Shprits (2009) suggests is most efficient for nearly equatorially mirroring electrons.

The presence of kinetic Alfven waves (KAWs) is highly likely, as the ratio of the low-frequency electric and magnetic perturbations almost equals the local Alfven speed ~10^6 m/s. Generation of KAWs is closely related to particle injections from the magnetotail. The parallel electric fields associated with KAWs can drive wave–particle interactions that trap electrons in a potential well and accelerate them along the field lines in the plasma sheet. The energy gain is limited to several kilo-electron volts (Artemyev et al., 2015) but may be a contributor toward the parallel potential drop pictured in Figure 5g. Additionally, parallel electric fields generated by electrostatic double layers can contribute toward accelerating electrons in the AAR. Parallel electric fields increase the parallel energy of the electrons—and therefore contribute to scattering them into the loss cone as well. Figure 5g indicates that the combined effect of energization processes between the ionosphere and the plasma sheet may accelerate electrons up to ~10 keV.

5. Conclusion

The current study demonstrates the utility of combining ISR-based measurement of energetic particle precipitation with conjugate spacecraft measurements. Our work begins to address a few specific unresolved problems in our understanding of substorm dynamic (1) the connection between ionospheric signatures and magnetotail processes; (2) energy transmission through the magnetosphere during substorms; and (3) location of the magnetospheric particle acceleration regions. The subrelativistic electron precipitation observed by PFISR, and its correlation with plasma sheet energetic electron flux measurements after the onset, suggests a direct link between the low altitude ionization and pitch angle scattering of these electrons from within the plasma sheet. The substorm onset originates very close to Poker Flat and primarily expands westward at an average rate of 2° per minute longitudinally. The substantial increase in fluxes of these electrons after the onset and large earthward convection during the onset suggest that they originate tailward of the location of THEMIS-D in the near-Earth plasma sheet and are likely energized by magnetotail reconnection.

In this particular substorm, the electron populations that transfer energy from the magnetosphere to the ionosphere were substantially different before and after the substorm onset. Before onset, the energy is transported predominantly by electrons $<$10 keV, which originate from pitch angle scattering within the plasma sheet. After onset, 75% or more of the energy flux is carried by electrons between 10 and 100 keV. They originate predominantly from pitch angle diffusion caused by parallel electric fields in the AAR and other processes that cause pitch angle scattering within and tailward of the AAR. We speculate the cause of the prolonged precipitation of subrelativistic electrons $>$100 keV after the onset of the substorm to be pitch angle scattering of these electrons in the plasma sheet and beyond ($\gtrsim 9R_E$) through bounce and cyclotron resonance with EMIC waves.

Key Findings

- Electron precipitation greater than ~100 keV after the onset originate tailward of the near-Earth plasma sheet
- Electrons between 10 and 100 keV are scattered into the loss cone by processes in and tailward of the AAR
- Cold electrons are accelerated up to 10 keV after the substorm onset by the parallel potential drop in the AAR

- Electron cyclotron and bounce interaction with EMIC waves within the plasma sheet may play a role in scattering subrelativistic electrons (≳100 keV) into the loss cone during the expansion phase of the substorm
- Measurements of electron density from ISR can be used to estimate the nighttime energy spectra of energetic electrons within the loss cone

Our work validates the ability of ISR measurements to estimate plasma sheet loss cone electron population reliably during a substorm. We hope to extend the ISR inversion technique to study two-dimensional transport of electron precipitation across the ionosphere using multibeam measurements made by electronically steerable ISRs such as PFISR. Furthermore, magnetically conjugate wave measurements from within the plasma sheet may allow us to estimate the average wave power required for scattering energetic electrons into the loss cone. Unlike spacecraft measurements, the ISR inversion technique provides remote measurements of the plasma sheet with good spatial and temporal coverage that one may use to carry out uninterrupted diagnostics of the phenomenon in question.

Acknowledgments

This work was supported by the Air Force Office of Scientific Research under contract FA9550-15-1-0503. The work of Y. Nishimura was supported by NASA grant NNX15AI62G and NNX15AI63G, NSF grant AGS-1451911 and PLR-1341359, and AFOSR grant FA9550-15-1-0179. The work of A. Kero was supported by the European Regional Development Fund (Regional Council of Lapland, decision number A70179). The authors wish to thank M. Hirsch, R. Marshall, A. Bhatt, S. Kaeppler, and E. Turunen for helpful discussions and J. Swoboda for enabling the use of the GeoDataMATLAB class to extract and plot ISR data (Swoboda et al., 2016). Additionally, we recognize the use of AIDA-tools (Gustavsson et al., 2016) to run the Monte Carlo simulations by Sergienko and Ivanov (1993). We acknowledge the use of ACE spacecraft data, obtained from NASA GSFC's Space Physics Data Facility OMNIWeb interface at https//omniweb.gsfc.nasa.gov. PFISR operations are supported by National Science Foundation Cooperative Agreement AGS-1133009 to SRI international. Processed PFISR data used are available in Madrigal database at https://isr.sri.com/madrigal. All data related to THEMIS are publically available at https://themis.ssl.berkeley.edu/data/themis/. We also acknowledge NASA contract NAS5-02099 and V. Angelopoulos for use of data from the THEMIS mission, and specifically S. Mende and E. Donovan for use of the ASI data, the CSA for logistical support in fielding and data retrieval from the GBO stations, and NSF for support of GIMNAST through grant AGS-1004736.

References

Albert, J. M. (2003). Evaluation of quasi-linear diffusion coefficients for EMIC waves in a multispecies plasma. *Journal of Geophysical Research*, *108*(A6), 1249. https//doi.org/10.1029/2002JA009792

Alfvén, H., & Fälthammar, C.-G. (1963). *Cosmical electrodynamic Fundamental principles* (2nd ed.). Oxford: Clarendon Press.

Anderson, K. A., & Enemark, D. C. (1960). Balloon observations of X rays in the auroral zone II. *Journal of Geophysical Research*, *65*(11), 3521–3538. https//doi.org/10.1029/JZ065i011p03521

Angelopoulos, V. (2008). The THEMIS mission. *Space Science Reviews*, *141*(1–4), 5–34. https://doi.org/10.1007/s11214-008-9336-1

Artemyev, A. V., Rankin, R., & Blanco, M. (2015). Electron trapping and acceleration by kinetic Alfven waves in the inner magnetosphere. *Journal of Geophysical Research: Space Physics*, *120*, 10,305–10,316. https//doi.org/10.1002/2015JA021781

Auster, H. U., Glassmeier, K. H., Magnes, W., Aydogar, O., Baumjohann, W., Constantinescu, D., … Wiedemann, M. (2008). The THEMIS Fluxgate Magnetometer. *Space Science Reviews*, *141*(1–4), 235–264. https://doi.org/10.1007/s11214-008-9365-9

Baker, D. N., Pulkkinen, T. I., Angelopoulos, V., Baumjohann, W., & McPherron, R. L. (1996). Neutral line model of substorm Past results and present view. *Journal of Geophysical Research*, *101*(A6), 12975. https//doi.org/10.1029/95JA03753

Barcus, J. R., & Rosenberg, T. J. (1966). Energy spectrum for auroral-zone X ray 1. Diurnal and type effects. *Journal of Geophysical Research*, *71*(3), 803–823. https//doi.org/10.1029/JZ071i003p00803

Berkey, F. T., Driatskiy, V. M., Henriksen, K., Hultqvist, B., Jelly, D. H., Shchuka, T. I., … Ylindemi, J. (1974). A synoptic investigation of particle precipitation dynamics for 60 substorms in IQSY (1964-1965) and IASY (1969). *Planetary and Space Science*, *22*(2), 255–307. https//doi.org/10.1016/0032-0633(74)90028-2

Birn, J., Artemyev, A. V., Baker, D. N., Echim, M., Hoshino, M., & Zelenyi, L. M. (2012). Particle acceleration in the magnetotail and aurora. *Space Science Reviews*, *173*(1–4), 49–102. https//doi.org/10.1007/s11214-012-9874-4

Bonnell, J. W., Mozer, F. S., Delory, G. T., Hull, A. J., Ergun, R. E., Cully, C. M., … Harvey, P. R. (2009). The Electric Field Instrument (EFI) for THEMIS. In *The THEMIS mission* (pp. 303–341). New York: Springer.

Borovsky, J. E. (1993). Auroral arc thicknesses as predicted by various theories. *Journal of Geophysical Research*, *98*(A4), 6101–6138. https//doi.org/10.1029/92JA02242

Boyle, C. B., Reiff, P. H., & Hairston, M. R. (1997). Empirical polar cap potentials. *Journal of Geophysical Research*, *102*(A1), 111–125. https//doi.org/10.1029/96JA01742

Brown, R. R. (1966). Electron precipitation in the auroral zone. *Space Science Reviews*, *5*(3), 311–387. https//doi.org/10.1007/BF02653249

Callis, L. B., Natarajan, M., Lambeth, J. D., & Baker, D. N. (1998). Solar atmospheric coupling by electrons (SOLACE): 2. Calculated stratospheric effects of precipitating electrons, 1979–1988. *Journal of Geophysical Research*, *103*(D21), 28421–28438. https//doi.org/10.1029/98JD02407

Censor, Y. (1981). Row-action methods for huge and sparse systems and their applications. *SIAM Review*, *23*(4), 444–466. https//doi.org/10.1137/1023097

Collis, P. N., & Korth, A. (1985). GEOS-2 observations of energetic electrons in the morning sector during auroral radio absorption events. *Journal of Atmospheric and Terrestrial Physics*, *47*(4), 327–339. https//doi.org/10.1016/0021-9169(85)90013-3

Colpitts, C. A., Hakimi, S., Cattell, C. A., Dombeck, J., & Maas, M. (2013). Simultaneous ground and satellite observations of discrete auroral arcs, substorm aurora, and Alfvénic aurora with FAST and THEMIS GBO. *Journal of Geophysical Research: Space Physics*, *118*, 6998–7010. https//doi.org/10.1002/2013JA018796

Dai, L., Wang, C., Duan, S., He, Z., Wygant, J. R., Cattell, C. A., … Tang, X. (2015). Near-Earth injection of MeV electrons associated with intense dipolarization electric field Van Allen Probes observations. *Geophysical Research Letters*, *42*, 6170–6179. https//doi.org/10.1002/2015GL064955

del Pozo, C. F., Burns, C. J., & Hargreaves, J. K. (1993). Dual-beam EISCAT radar observations of the dynamics of the disturbed *D*- and *E*-regions in the early morning sector. *Journal of Atmospheric and Terrestrial Physics*, *55*(10), 1393–1415. https://doi.org/10.1016/0021-9169(93)90107-A

Fang, X., Lummerzheim, D., & Jackman, C. H. (2013). Proton impact ionization and a fast calculation method. *Journal of Geophysical Research: Space Physics*, *118*, 5369–5378. https//doi.org/10.1002/jgra.50484

Gabrielse, C., Angelopoulos, V., Runov, A., & Turner, D. L. (2012). The effects of transient, localized electric fields on equatorial electron acceleration and transport toward the inner magnetosphere. *Journal of Geophysical Research*, *117*, A10213, https//doi.org/10.1029/2012JA017873

Ganguli, G., Palmadesso, P. J., Fedder, J., & Lui, A. T. Y. (1995). Role of Fermi acceleration in explosive enhancement of cross-tail current in late substorm growth phase. *Geophysical Research Letters*, *22*(17), 2405–2408. https//doi.org/10.1029/95GL02488

Gustavsson, B., Brändström, U., & Hirsch, M. (2016). AIDA-tool ALIS auroral tomography Matlab software suite [Data Set], https://doi.org/10.5281/zenodo.213308.

Hada, T., Nishida, A., Teresawa, T., & Hones, E. W. (1981). Bi-directional electron pitch angle anisotropy in the plasma sheet. *Journal of Geophysical Research*, *86*(A13), 11211. https//doi.org/10.1029/JA086iA13p11211

Hartz, T. R., & Brice, N. M. (1967). The general pattern of auroral particle precipitation. *Planetary and Space Science*, *15*(2), 301–329. https//doi.org/10.1016/0032-0633(67)90197-3
Hysell, D. L. (2007). Inverting ionospheric radio occultation measurements using maximum entropy. *Radio Science*, *42*, RS4022, https//doi.org/10.1029/2007RS003635
Imhof, W. L., Reagan, J. B., & Gaines, E. E. (1978). The energy selective precipitation of inner zone electrons. *Journal of Geophysical Research*, *83*(A9), 4245. https//doi.org/10.1029/JA083iA09p04245
Kirkwood, S., & Eliasson, L. (1990). Energetic particle precipitation in the substorm growth phase measured by EISCAT and Viking. *Journal of Geophysical Research*, *95*(A5), 6025. https//doi.org/10.1029/JA095iA05p06025
Kirkwood, S., & Osepian, A. (1995). Quantitative studies of energetic particle precipitation using Incoherent Scatter Radar. *Journal of Geomagnetism and Geoelectricity*, *47*(8), 783–799. https//doi.org/10.5636/jgg.47.783
Kosch, M. J., Honary, F., del Pozo, C. F., Marple, S. R., & Hagfors, T. (2001). High-resolution maps of the characteristic energy of precipitating auroral particles. *Journal of Geophysical Research*, *106*(A12), 28,925–28,937. https//doi.org/10.1029/2001JA900107
Kurita, S., Kadokura, A., Miyoshi, Y., Morioka, A., Sato, Y., & Misawa, H. (2015). Relativistic electron precipitations in association with diffuse aurora: Conjugate observation of SAMPEX and the all-sky TV camera at Syowa Station. *Geophysical Research Letters*, *42*, 4702–4708. https//doi.org/10.1002/2015GL064564
Lam, M. M., Horne, R. B., Meredith, N. P., Glauert, S. A., Moffat-Griffin, T., & Green, J. C. (2010). Origin of energetic electron precipitation $<$30 keV into the atmosphere. *Journal of Geophysical Research*, *115*, A00F08. https//doi.org/10.1029/2009JA014619
Lennartsson, W. (1987). Plasma sheet ion composition at various levels of geomagnetic and solar activity. *Physica Scripta*, *36*(2), 367–371. https//doi.org/10.1088/0031-8949/36/2/029
Lopez, R. E. (2000). The current sheet disruption model for substorm expansion phase onset: Background, arguments, and relationship to global substorm evolution. *Advances in Space Research*, *25*(7–8), 1667–1677. https//doi.org/10.1016/S0273-1177(99)00682-1
Lorentzen, K. R., McCarthy, M. P., Parks, G. K., Foat, J. E., Millan, R. M., Smith, D. M., … Treilhou, J. P. (2000). Precipitation of relativistic electrons by interaction with electromagnetic ion cyclotron waves. *Journal of Geophysical Research*, *105*(A3), 5381–5389. https//doi.org/10.1029/1999JA000283
Lui, A. T. Y., Venkatesan, D., Anger, C. D., Akasofu, S.-I., Heikkila, W. J., Winningham, J. D., & Burrows, J. R. (1977). Simultaneous observations of particle precipitations and auroral emissions by the Isis 2 satellite in the 19-24 MLT sector. *Journal of Geophysical Research*, *82*(16), 2210–2226. https//doi.org/10.1029/JA082i016p02210
McDiarmid, I. B., Burrows, J. R., & Budzinski, E. E. (1975). Average characteristics of magnetospheric electrons (150 eV to 200 keV) at 1400 km. *Journal of Geophysical Research*, *80*(1), 73–79. https//doi.org/10.1029/JA080i001p00073
Mende, S. B., Harris, S. E., Frey, H. U., Angelopoulos, V., Russell, C. T., Donovan, E., … Peticolas, L. M. (2008). The THEMIS array of ground-based observatories for the study of auroral substorms. *Space Science Reviews*, *141*(1–4), 357–387. https//doi.org/10.1007/s11214-008-9380-x
Meredith, L. H., Gottlieb, M. B., & Van Allen, J. A. (1955). Direct detection of soft radiation above 50 kilometers in the auroral zone. *Physics Review*, *97*(1), 201–205. https//doi.org/10.1103/PhysRev.97.201
Mironova, I. A., Aplin, K. L., Arnold, F., Bazilevskaya, G. A., Harrison, R. G., Krivolutsky, A. A., … Usoskin, I. G. (2015). Energetic particle influence on the Earth's atmosphere. *Space Science Reviews*, *194*(1–4), 1–96. https//doi.org/10.1007/s11214-015-0185-4
Morley, S. K., Friedel, R. H. W., Cayton, T. E., & Noveroske, E. (2010). A rapid, global and prolonged electron radiation belt dropout observed with the Global Positioning System constellation. *Geophysical Research Letters*, *37*, L06102. https//doi.org/10.1029/2010GL042772
Osepian, A., Kirkwood, S., & Smirnova, N. (1996). Energetic electron precipitation during auroral events observed by incoherent scatter radar. *Advances in Space Research*, *17*(11), 149–155. https//doi.org/10.1016/0273-1177(95)00743-X
Parks, G. K., McCarthy, M., Fitzenreiter, R. J., Etcheto, J., Anderson, K. A., Anderson, R. R., … Williams, D. J. (1984). Particle and field characteristics of the high-latitude plasma sheet boundary layer. *Journal of Geophysical Research*, *89*(A10), 8885. https//doi.org/10.1029/JA089iA10p08885
Pytte, T., & West, H. I. (1978). Ground-satellite correlations during presubstorm magnetic field configuration changes and plasma sheet thinning in the near-Earth magnetotail. *Journal of Geophysical Research*, *83*(A8), 3791. https//doi.org/10.1029/JA083iA08p03791
Roux, A., Le Contel, O., Coillot, C., Bouabdellah, A., de la Porte, B., Alison, D., … Vassal, M. C. (2008). The Search Coil Magnetometer for THEMIS. *Space Science Reviews*, *141*(1–4), 265–275. https://doi.org/10.1007/s11214-008-9455-8
Semeter, J., & Kamalabadi, F. (2005). Determination of primary electron spectra from incoherent scatter radar measurements of the auroral e region. *Radio Science*, *40*, RS2006. https://doi.org/10.1029/2004RS003042
Semeter, J., Butler, T. W., Zettergren, M., Heinselman, C. J., & Nicolls, M. J. (2010). Composite imaging of auroral forms and convective flows during a substorm cycle. *Journal of Geophysical Research*, *115*, A08308. https://doi.org/10.1029/2009JA014931
Seppälä, A., Clilverd, M. A., Beharrell, M. J., Rodger, C. J., Verronen, P. T., Andersson, M. E., & Newnham, D. A. (2015). Substorm-induced energetic electron precipitation: Impact on atmospheric chemistry. *Geophysical Research Letters*, *42*, 8172–8176. https://doi.org/10.1002/2015GL065523
Sergienko, T. I., & Ivanov, V. E. (1993). A new approach to calculate the excitation of atmospheric gases by auroral electron impact. *Annales de Geophysique*, *11*(8), 717–727.
Shprits, Y. Y. (2009). Potential waves for pitch-angle scattering of near-equatorially mirroring energetic electrons due to the violation of the second adiabatic invariant. *Geophysical Research Letters*, *36*, L12106. https://doi.org/10.1029/2009GL038322
Swoboda, J., Hirsch, M., Lee, A., & Semeter, J. (2016). jswoboda/GeoDataMATLAB: ISR Sim Paper [Data Set]. https://doi.org/10.5281/ZENODO.154536
Tanskanen, P. J., Hardy, D. A., & Burke, W. J. (1981). Spectral characteristics of precipitating electrons associated with visible aurora in the premidnight oval during periods of substorm activity. *Journal of Geophysical Research*, *86*(A3), 1379–1395. https://doi.org/10.1029/JA086iA03p01379
Thorne, R. M., O'Brien, T. P., Shprits, Y. Y., Summers, D., & Horne, R. B. (2005). Timescale for MeV electron microburst loss during geomagnetic storms. *Journal of Geophysical Research*, *110*, A09202. https://doi.org/10.1029/2004JA010882
Tsyganenko, N. A. (1989). A magnetospheric magnetic field model with a warped tail current sheet. *Planetary and Space Science*, *37*(1), 5–20. https://doi.org/10.1016/0032-0633(89)90066-4
Turunen, E., Matveinen, H., Tolvanen, J., & Ranta, H. (1996). *D*-region ion chemistry model. In R. W. Schunk (Ed.), *STEP handbook of ionospheric models* (pp. 1–25). Boulder, CO: SCOSTEP Secretariat.
Turunen, E., Kero, A., Verronen, P. T., Miyoshi, Y., Oyama, S.-I., & Saito, S. (2016). Mesospheric ozone destruction by high-energy electron precipitation associated with pulsating aurora. *Journal of Geophysical Research: Atmospheres*, *121*, 11,852–11,861. https://doi.org/10.1002/2016JD025015

Verronen, P. T., Seppälä, A., Clilverd, M. A., Rodger, C. J., Kyrölä, E., Enell, C.-F., … Turunen, E. (2005). Diurnal variation of ozone depletion during the October–November 2003 solar proton events. *Journal of Geophysical Research*, *110*, A09S32. https://doi.org/10.1029/2004JA010932

Verronen, P. T., Andersson, M. E., Kero, A., Enell, C.-F., Wissing, J. M., Talaat, E. R., … Armandillo, E. (2015). Contribution of proton and electron precipitation to the observed electron concentration in October–November 2003 and September 2005. *Annales de Geophysique*, *33*(3), 381–394. https://doi.org/10.5194/angeo-33-381-2015

Vickrey, J. F., Vondrak, R. R., & Matthews, S. J. (1982). Energy deposition by precipitating particles and Joule dissipation in the auroral ionosphere. *Journal of Geophysical Research*, *87*(A7), 5184–5196. https://doi.org/10.1029/JA087iA07p05184

Wang, C. P., Zaharia, S. G., Lyons, L. R., & Angelopoulos, V. (2013). Spatial distributions of ion pitch angle anisotropy in the near-Earth magnetosphere and tail plasma sheet. *Journal of Geophysical Research*, *118*, 244–255. https://doi.org/10.1029/2012JA018275

Zettergren, M., Semeter, J., Blelly, P.-L., Sivjee, G., Azeem, I., Mende, S., … Witasse, O. (2008). Optical estimation of auroral ion upflow: 2. A case study. *Journal of Geophysical Research*, *113*, A07308. https://doi.org/10.1029/2008JA013135